A multi-method analysis of Si-, S- and *REE*-rich apatite from a new find of kalsilite-bearing leucitite (Abruzzi, Italy)

P. Comodi[1], Y. Liu[2], F. Stoppa[3] and A.R. Woolley[4]

[1] Dipartimento di Scienze della Terra, Università di Perugia, 06100-Perugia, Italy
[2] Wuhan Institute of Chemical Technology, 430073-Wuhan, P.R. China
[3] Dipartimento di Scienze della Terra, Università G. d'Annunzio, 66013-Chieti Scalo, Italy
[4] Department of Mineralogy, Natural History Museum, Cromwell Road, London SW7 5BD, UK

ABSTRACT

The crystal chemistry characteristics of a hydroxyl-fluor apatite from a recently discovered kalsilite-bearing leucitite from Abruzzi, Italy, were investigated by electron microprobe, single crystal X-ray diffraction, IR, Raman and micro-Raman spectroscopy. The apatite has exceptionally high S and relatively high Si, Sr and *LREE*, whereas the *HREE* content is negligible. The IR spectra confirm the presence of OH calculated from formula difference. A high positive correlation between Ca-site Substitution Index (CSI = 100(10-Ca)/Ca) and Tetrahedral Substitution Index (TSI = 100 (Si+C+S)/P atom/a.p.f.u.) and a systematic parallel increase in *REE*, S and Si indicate two substitution mechanisms, i.e. $REE^{3+} + Si^{4+} = Ca^{2+} + P^{5+}$ and $Si^{4+} + S^{6+} = 2 P^{5+}$. Site occupancy data and bond lengths, determined from structural refinements on selected samples, demonstrate that *LREE* and Sr show a marked preference for the Ca2 site, even though in the *LREE*-rich samples a partial substitution of *LREE* for Ca in the Ca1 site was observed.

Tetrahedral distances (from 1.535 to 1.541 Å) reflect the substitution of Si^{4+} and S^{6+} for P^{5+}, which is also confirmed by vibrational spectra. As $(SiO_4)^{4-}$ and $(SO_4)^{2-}$ substitute for $(PO_4)^{3-}$, the relative intensity of v_1 Raman bands of $(SO_4)^{2-}$ (at 1007 cm^{-1}) and $(SiO_4)^{4-}$ (at 865 cm^{-1}) increase systematically, while that of phosphate decreases and the five components of phosphate v_3 modes disappear. Moreover, the $(PO_4)^{3-}$ Raman peak broadening is linearly correlated with the Si and S concentrations.

Apatite crystals are sometimes zoned with compositions varying from SiO_2 = 1.15–2.07 wt.%, $\Sigma(LREE_2O_3)$ = 0.56–1.08 wt.% and SrO = 0.58–1.02 wt.% in the core to 3.98–5.03, 4.14–6.73 and 1.97–2.17, respectively, in the rim. A sharp, strong enrichment in Sr and *LREE* in the rim indicate that the apatite suddenly became an acceptor of these elements in the late stages of crystallization.

Introduction

APATITE is one of the most important accessory minerals of alkaline rocks and carbonatites. It readily accommodates incompatible and volatile elements under a wide range of *P-T* conditions, reflecting magma crystallization conditions (Watson and Green, 1981; Roeder *et al.*, 1987; Farver and Giletti, 1989; Ronsbo, 1989; Stoppa and Liu, 1995; Deer *et al.*, 1996). Apatite from leucitites, melilitites and carbonatites belonging to the Intramountain Ultra-alkaline Province of

Italy (IUP of Lavecchia and Stoppa, 1996) were investigated by Liu and Comodi (1993) and by Stoppa and Liu (1995). The present study adds information to a new find of apatite from IUP, occurring at Grotta del Cervo, Abruzzi, Italy (Stoppa and Woolley, in prep). This apatite is of interest for its unusual composition which is extreme among IUP apatites. The *LREE*$_2O_3$ in the Grotta del Cervo apatite is up to 6 wt.% and is distinctly higher than the value of 1 wt.% reported for other IUP apatites (Stoppa and Liu, 1995). The *LREE* content in apatite broadly correlates with Sr

(Exley and Smith, 1982), which is up to 2% in the Grotta del Cervo apatite. In addition, S in the Grotta del Cervo apatite ranges between 1.5 and 3.5 wt.%, mostly higher than the S range reported from other IUP apatites which yielded S as high as 1.64 wt.% (Liu and Comodi, 1993). Notably, apatite from volcanic rocks generally contains very low concentrations of S (0.04–0.89 wt.%: Nash, 1983).

The observed amount of S, *LREE* and Sr implies important modifications in the crystal structure (Hughes *et al.*, 1989,1991; Fleet and Pan, 1995). Sulphate and silicate ions may substitute for phosphate to form a solid solution series of silicic sulphatic apatite (Khorari *et al.*, 1994). The charge increase owing to substitution of Ca^{2+} by REE^{3+} is electrostatically compensated by the concomitant substitution of Na^+ for Ca^{2+} and Si^{4+} for P^{5+}.

Vibrational spectra are sensitive to change of structural environment and ion-substitution in crystals. The infrared (IR) and Raman spectra characteristics of apatite are mainly represented by the vibrational modes of the tetrahedral anions PO_4, SiO_4, SO_4 and CO_3. For example, IR spectroscopy has been widely used to distinguish the existence of structural carbonate and to determine its amount in the apatite structure (Featherstone *et al,.* 1984; Regnier *et al.*, 1994; Santos and Clayton, 1995). Based on the same principle, the influences of Si and S substitution for P in the apatite structure should be reflected in its vibrational spectra as well as in the tetrahedral geometry.

The above features have been demonstrated to be a useful tool for inferring possible ultra-alkaline evolution processes in the petrogenesis of such rocks (Stoppa and Liu, 1995). In this paper, X-ray diffraction and vibrational spectroscopy data from a widely Ca- and P-site substituted hydroxy-fluorapatite from Abruzzi, Italy, is compared with its chemical composition. The influence of ion substitution in the apatite structure on its vibrational properties is discussed.

Geological setting and sample preparation

Grotta del Cervo is located ~60 km NE of Rome in a small graben structure along a system of normal faults trending NE–SW and N–S. The occurrence consists of reworked tuff containing fresh blocks of lava which fill up some sections of a karst cave. The vent area has not been identified but relatively large blocks point to a local origin.

The age of the igneous activity is inferred to fall between 0.8 and 0.3 m.y. The lava blocks consist principally of large crystals of phlogopite, leucite, haüyne and clinopyroxene in a fine groundmass of melanite, apatite, spinel and kalsilite. The associated tuff contains variable amounts of the same minerals observed in the lava plus secondary calcite. Apatite crystals form hexagonal prisms terminated by pyramidal faces, up to several hundred μm along the *c*-axis and 20–50 μm across the *c*-axis (Fig. 1).

Some single crystals, without visible inclusions, were carefully hand-picked after separation (see Liu and Comodi 1993, for separation technique) and preliminary analyses carried out, using an energy dispersive system (EDS) on a scanning electron microscope (SEM). Four crystals (CG1, CG5, CG6, CG7) were selected as representative of the compositional range and subdivided into several fragments suitable for X-ray diffraction, electron microprobe analysis (EMPA) and micro-Raman spectroscopy.

The fluorapatite of Durango, Mexico (DA3), which has been widely used as an analytical reference standard (Young *et al.*, 1969) and an ellestadite sample from Crestmore, California (U.S. National Museum of Natural History, NMNH # 103072, Rouse and Dunn, 1982), were investigated as end-members for P substitution by Si and S. We collected structural and Raman data for the Durango apatite but only the Raman spectra for the ellestadite, for which we used the structural data of Hughes and Drexler (1991).

The chemical compositions of six crystals (A to F), in two thin sections, were determined by Electron Microprobe Analysis (EMPA).
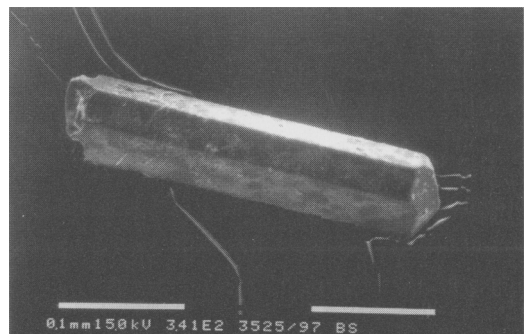

FIG. 1. Secondary electron images of Abruzzi hydroxyl-fluorapatite.

TABLE 1. Representative chemical analyses of Grotta del Cervo apatite, with OH anions (*) calculated from the difference in the structure column

Sample codes	A(core)	B(core)	B(rim)	C(core)	C(rim)	D(core)	D(rim)	E(core)	E(rim)	F(core)	CG1	CG5	CG6	CG7
CaO	54.73	54.81	51.50	54.22	49.97	54.15	48.58	54.15	51.62	54.39	54.61	55.53	51.76	55.34
SrO	0.59	0.58	2.04	1.12	2.02	1.02	1.97	0.81	2.17	0.85	1.57	0.60	1.77	0.61
FeO	0.04	0.11	0.13	0.05	0.11	0.04	0.08	0.06	0.08	0.06	0.04	n.d.	n.d.	0.07
MgO	0.07	0.05	n.d.	n.d.	n.d.	n.d.	n.d.	0.03	0	0.04	n.a.	n.a.	n.a.	n.a.
MnO	n.d.	0.04	0.03	n.d.	n.d.	n.d.	0.04	n.d.	0	n.d.	n.a.	n.a.	n.a.	n.a.
BaO	0.02	0.03	0.05	0.02	0.04	0.02	0.03	0.10	0.06	0.04	n.a.	n.a.	n.a.	n.a.
Na$_2$O	0.06	0.06	0.07	0.09	0.09	0.08	0.11	0.10	0.06	0.10	0.06	0.24	0.06	0.07
La$_2$O$_3$	0.09	0.15	1.39	0.17	2.29	0.25	2.43	0.19	2.06	0.21	0.86	1.21	1.36	0.14
Ce$_2$O$_3$	0.28	0.29	2.40	0.43	3.69	0.62	3.78	0.47	3.09	0.49	1.58	2.00	2.51	0.30
Nd$_2$O$_3$	0.13	0.12	0.35	0.13	0.47	0.21	0.52	0.21	0.46	0.13	0.48	0.33	0.92	0.11
Pr$_2$O$_3$	0.03	n.d.	0.15	n.d.	0.25	n.d.	0.24	0.04	0.11	0.04	n.a.	n.a.	n.a.	n.a.
Sm$_2$O$_3$	n.d.	0.09	n.d.	0.03	n.d.	0.08	n.d.	0.04	0.04	n.d.	n.a.	n.a.	n.a.	n.a.
Y$_2$O$_3$	n.d.	0.03	0.07	0.05	n.d.	0.04	0.04	0.04	0.04	0.02	n.a.	n.a.	n.a.	n.a.
Al$_2$O$_3$	n.d.	0.03	0.07	0.02	0.03	0.04	0.03	0.04	0.04	0.04	n.a.	n.a.	n.a.	n.a.
P$_2$O$_5$	38.75	37.60	32.29	37.29	29.63	37.11	29.58	37.21	31.07	36.85	34.22	30.09	31.68	38.22
SiO$_2$	1.41	1.85	3.98	1.72	5.03	2.07	4.88	1.80	4.75	1.86	3.11	4.39	3.94	1.15
SO$_3$	1.62	1.83	2.57	1.87	1.93	2.15	2.24	1.88	1.67	1.93	1.53	3.50	1.60	0.92
F	2.42	2.41	2.46	2.45	2.18	2.36	2.64	2.61	1.78	2.48	1.46	2.00	2.20	1.87
Cl	0.01	0.01	0.02	0.01	0.02	0.01	0.03	0.03	0.02	0.03	0.02	0.01	0.02	0.05
H$_2$O	0.72	0.70	0.74	0.67	0.66	0.73	0.38	0.59	0.90	0.65	1.10	0.85	0.69	0.94
O=F,Cl	1.02	1.02	1.05	1.04	0.92	1.00	1.12	1.10	0.75	1.05	0.61	0.84	0.93	0.78
Sum	99.97	99.74	99.04	99.32	97.49	99.98	96.48	99.22	99.23	99.18	99.99	99.92	97.59	99.01
Atom number														
Ca	9.65	9.73	9.51	9.68	9.57	9.61	9.70	9.68	9.66	9.74	9.90	10.11	9.76	9.91
Sr	0.05	0.05	0.20	0.11	0.21	0.10	0.21	0.08	0.21	0.08	0.15	0.06	0.18	0.06
Na	0.02	0.02	0.02	0.03	0.03	0.03	0.04	0.03	0.02	0.03	0.02	0.08	0.02	0.02
La	−0.01	0.01	0.09	0.01	0.15	0.01	0.16	0.01	0.13	0.01	0.05	0.07	0.09	0.01
Ce	0.02	0.02	0.15	0.03	0.24	0.04	0.25	0.03	0.19	0.03	0.10	0.12	0.16	0.02
Nd	−0.01	0.01	0.02	0.01	0.03	0.01	0.03	0.01	0.03	0.01	0.03	0.02	0.06	0.01
P	5.29	5.15	4.62	5.16	4.40	5.10	4.58	5.15	4.50	5.11	4.81	4.24	4.63	5.30
Si	0.23	0.30	0.67	0.28	0.88	0.34	0.89	0.29	0.81	0.31	0.52	0.73	0.68	0.19
S	0.20	0.22	0.33	0.23	0.25	0.26	0.31	0.23	0.21	0.24	0.19	0.44	0.21	0.11
F	1.22	1.24	1.32	1.27	1.21	1.21	1.53	1.35	0.96	1.28	0.77	1.05	1.20	0.97
Cl	−0.01	−0.01	0.01	−0.01	0.01	−0.01	0.01	0.01	0.01	0.01	0.01	−0.01	0.01	0.01
OH*	0.78	0.76	0.67	0.73	0.78	0.79	0.46	0.64	1.03	0.71	1.22	0.95	0.79	1.02

n.a.: not analysed, n.d.: not detected

TABLE 2. Details of data collections, structural refinements and selected structural parameters

	DA3	CG7	CG1	CG6
a (Å)	9.3926	9.3995	9.4035	9.4117
c (Å)	6.8828	6.8877	6.8990	6.9082
V (Å^3)	525.86	527.00	528.32	529.95
n. measured reflections	1568	1609	1218	1099
n. independent reflections	682	730	572	524
n. parameters	44	43	43	43
R equivalent %	2.6	2.1	2.5	2.3
R %	2.1	2.6	4.4	2.8
P−O3 (x2)	1.534 (1)	1.534 (1)	1.542 (3)	1.542 (2)
P−O1	1.534 (1)	1.535 (2)	1.530 (3)	1.536 (2)
P−O2	1.540 (1)	1.540 (2)	1.542 (3)	1.543 (2)
<P−O>	1.535	1.536	1.539	1.541
Ca1−O1 (x3)	2.401 (1)	2.401 (1)	2.411 (3)	2.411 (2)
Ca1−O2 (x3)	2.455 (1)	2.455 (2)	2.460 (3)	2.458 (2)
Ca1−O3 (x3)	2.807 (1)	2.807 (2)	2.808 (3)	2.816 (2)
<Ca1−O>	2.554	2.554	2.560	2.562
Ca2−F	2.307 (1)	2.325 (1)	2.317 (3)	2.315 (1)
Ca2−O3 (x2)	2.350 (1)	2.348 (2)	2.352 (3)	2.352 (2)
Ca2−O2	2.378 (1)	2.369 (2)	2.375 (3)	2.389 (3)
Ca2−O3' (x2)	2.498 (1)	2.505 (2)	2.502 (3)	2.514 (2)
Ca2−O1	2.696 (1)	2.699 (2)	2.685 (3)	2.685 (2)
<Ca2−O>	2.462	2.462	2.461	2.468

Analytical techniques

Electron microprobe analysis (EMPA)

Samples CG1, CG5, CG6 and CG7 were analysed for Ca, Sr, Na, La, Ce, Nd, P, Si, S, F and Cl using a CAMECA/CAMEBAX electron microprobe system (Centro Studi per i problemi dell'Orogeno, Alpi Orientali, C.N.R., Padova, Italy), using natural apatite as a standard for P, F and Ca; albite for Na; wollastonite for Si; blende for S; celestine for Sr; vanadinite for Cl and synthetic rare earth glass for La, Ce and Nd. The accelerating voltage was 15 kV and the beam current, 20 nA. The peak and background count times were 10 and 5 s, respectively, for all elements except the LREE, for which 20 and 7 s applied. The compositional data shown in Table 1 are the mean values of 4−8 representative analyses.

The apatite crystals in the rock thin sections, labelled A−F were analysed for Ca, Sr, Ba, Fe, Mg, Mn, Na, La, Ce, Pr, Nd, Sm, Y, Al, P, Si, S, F and Cl with a CAMECA SX50 electron microprobe at the Department of Mineralogy, Natural History Museum, London. The analyses were carried out at 15 kV and 20 nA, using a natural apatite as standard for P and F; wollastonite for Si and Ca; celestine for S; synthetic Sr, Ti oxide for Sr; synthetic rare earth glass for LREE; jadeite for Na; halite for Cl, corundum for Al, olivine for Mg, pure metals for Fe and Mn, and barium fluoride for Ba. Peak and background count times were 20−50 and 10−30 s respectively. For crystals B, C, D and E, analyses on both crystal cores and rims were carried out. The compositions are given in Table 1.

Structural formulae were calculated by assuming 10 cations in the Ca site. The OH ion was calculated by normalization of ideal stoichiometry in column anions (F+Cl+OH = 2). As there are no detectable bands for structural carbonate in the IR spectra of the investigated samples, CO_3 was regarded as negligible.

Structural refinement

With the exception of CG5, poor crystallinity inhibited collection of good quality diffraction data. Intensity data for CG1, CG6, CG7 and DA3 were collected on a Philips PW1100 single-crystal

diffractometer using graphite-monochromatized Mo-$K\alpha$ radiation. The $\pm$ $h+k+l$ reflections were collected, within the $0-40°\theta$ range, with ω scan and a scan width of 1.6°. Absorption was corrected using the semi-empirical method of North *et al.* (1968). The structure was refined in the $P6_3/m$ space group using the SHELXL93 package (Sheldrick, 1993). Full-matrix least squares refinement was performed by refining positional parameters, scale factors, anisotropic temperature factors for atoms, extinction factor, weight and site occupancies for the Ca1 and Ca2 sites. In the Abruzzi samples rare earth atoms were modelled with a Ce scattering factor, as Ce is the most abundant *REE* in these apatites. Owing to the uncertainty of *REE* analysis by electron microprobe, we refined site occupancies of Ca1 and Ca2 sites and then compared the structural occupancy with the chemical data.

Table 2 shows details of data collection and refinements for some selected structural data. Positional parameters, anisotropic temperature factors and observed-calculated structure factors can be obtained from the Principal Editor.

Infrared (IR) spectroscopy

Two milligrams of carefully hand-picked Abruzzi apatite crystals were mixed with 200 mg of KBr and ground in an agate mortar. A pellet was prepared in a die with a 1.27 cm diameter under vacuum at a pressure of 200 kg/cm^2 and heated overnight at 110°C to avoid absorption of atmospheric moisture. The spectrum was obtained using an FTIR instrument, BRUKER IFS113V, collecting 100 scans in vacuum ($P = 5$ mbar) over the range $400-4000$ cm^{-1} with a resolution of 2 cm^{-1}. The estimated wavenumber accuracy is ~1 cm^{-1}.

Raman and Raman microprobe (RM) spectroscopy

Polarized Raman spectra of the CG7, Durango and ellestadite samples were obtained using a 90° geometry. An argon laser, COHERENT INNOVA 400, at the Chemistry Department, University of Perugia, was used as a light source, with an excitation of 514.5 nm. The scattered radiation was analysed using a Jobin-Yvon spectrometer U1000, with 1.3 cm^{-1} resolution. The signal was detected using a Thorn-Enn photomultiplier R943XXM, thermoelectrically cooled to 30°C.

Fragments of crystals CG1, CG5 and CG6 were selected for RM measurement at the European Non-Linear Spectroscopic Laboratory, Florence,

Italy. A Kr ion laser, COHERENT INNOVA 300, with an excitation of 641.7 nm, was adopted as the light source. The laser beam with a diameter of several µm was focused on the randomly orientated crystal surfaces. The scattered radiation was analysed using a Jobin-Yvon spectrometer 3000, with a 3 cm^{-1} resolution. The signals were recorded under 180° backscattering geometry and were detected using a CCD type detector. The estimated wavenumber accuracy is ~2 cm^{-1}.

A curve-fitting technique was applied for the precise frequency determination of the Raman bands for all samples. The intensity, expressed as integrated area, and the peak width at half-height, were obtained using a curve fitting program.

Results

EMPA

The analytical data (Table 1) indicate that the apatite is unusually rich in Sr (SrO = $0.58-2.17$ wt.%), Si (SiO$_2$=$1.15-5.03$ wt.%), S (SO$_3$=$0.92-3.90$ wt.%) and *LREE*, i.e. the sum of La, Ce and Nd oxides ($\Sigma LREE_2O_3$ = $0.50-6.73$ wt.%), and contains negligible Y, Sm and Pr and other *HREE*. Elements such as Fe, Mg, Mn, Ba and Al are also negligible. Sodium occurs in all analyses but Na$_2$O is generally <0.1 wt.%. Fluorine is the principal anion and varies from 1.46 to 2.64 wt.%. Chlorine is negligible (Cl<0.05 wt.%). Formula calculations indicate the existence of an hydroxyl anion or a vacancy.

The EMPA analysis of the thin-sections indicated compositional zonation in some apatite crystals, with generally very thin outer zones (<10 µm), and commonly interstitial with the surrounding minerals. The compositional differences between cores and rims are noteworthy. Core SrO increases from ~1 wt.% to ~2 wt.% in rims; $\Sigma(LREE_2O_3)$ from <1 wt.% to >4 wt.%, with a sharp *LREE* enrichment in the rim (core La$_2$O$_3$/Nd$_2$O$_3$=$0.69-1.61$; rim La$_2$O$_3$/Nd$_2$O$_3$ = $3.97-4.87$; core SiO$_2$ <2 wt.%, but $4-5$ wt.% in the rim. There is a systematic reduction of CaO (from ~55 wt.% to ~50 wt.%) and P$_2$O$_5$ (from ~37 wt.% to ~31 wt.%) from core to rim, indicating a wider Ca-site and tetrahedral substitutions in the late stages of apatite crystallization.

Structural refinements

The apatite structure (space group $P6_3/m$) can be described with Ca1, nine-fold coordinated and

Ca2 seven-fold coordinated polyhedra, forming columns around the central [001] hexad, where F, Cl and OH ions are located. Adjacent Ca1 and Ca2 polyhedra are linked through oxygen atoms shared with PO_4 tetrahedra.

Of the different substitutions that may affect the PO_4 group, namely SiO_4, SO_4, CO_3, VO_4, AsO_4 etc., only Si and S were detectable in the studied samples. The effects of Si and S substitution of P are opposite ($^{[4]}S-O = 1.49$ Å, $^{[4]}Si-O = 1.61$ Å; International Tables for X-ray Crystallography, V, II, 1967). In our structural refinements we observed a linear increase of mean <P−O> bond length with (Si-S) content (Tables 1 and 2): <P−O> is 1.535 Å in DA3 where the Si and S contents are negligible and became 1.541 Å in CG6 where Si-S is 0.46 a.p.f.u. These values interpolate well the relationship between the mean <P−O> bond lengths and the Si content found in the literature (Hughes et al., 1991, Fig. 4).

Calcium in Ca1 and Ca2 polyhedra may be substituted by Na, K, Ag, Sr, Cd, REE, U etc. In the investigated samples, Ca is substituted mainly by LREE and in part by Sr, whereas other cations, like Na, are negligible. The distribution of REE has been addressed in numerous studies, e.g. Hughes et al. (1991) and Fleet and Pan (1995, 1997).

Fleet and Pan (1995) demonstrated that the Ca2 position in apatite is underbonded and, therefore, minor amounts of trivalent REE should favour Ca2 over Ca1 to increase the bond valence of Ca.

The results of occupancy refinements of the Ca1 and Ca2 sites in all CG samples indicate that the number of electrons in both sites is greater than that ascribed to the Ca atom alone. The REE occupancy, modelled with the Ce scattering factor, indicate a marked preference of REE for the Ca2 site, if the REE are not excluded from either Ca sites. The ratio of REE_{Ca2}/REE_{Ca1} in CG samples varies between 2.8 and 5, increasing with decreasing REE content.

In the apatites studied by Hughes et al. (1991), with a total REE content varying from 1.26 to 0.33 a.p.f.u., the REE_{Ca2}/REE_{Ca1} ratio changed from 1.76 to 3.00. Thus our results indicate the same relationship described by Hughes et al. (1991), i.e. REE content and REE_{Ca2}/REE_{Ca1} ratio are inversely correlated.

IR spectroscopy

The IR spectra of the samples contain four groups of bands due to phosphate ions, in good

agreement with the theoretical prediction (Kravitz et al., 1968; Klee, 1970). The v_1 (PO_4) mode occurs at 963 cm^{-1}. The $v_2(PO_4)$ mode is doubly degenerated and only a poorly resolved wide band could be detected near 468−474 cm^{-1}. The $v_3(PO_4)$, v_4 (PO_4) modes are both triply degenerated and only two bands at 1092 and 1041 cm^{-1} for the v_3 (PO_4) and two at 602 and 573 cm^{-1} for v_2 (PO_4) could be resolved.

As well as the phosphate bands, a set of bands due to SiO_4 and SO_4 ions were observed: bands at 1161 and 648 cm^{-1} may be assigned to SO_4 and bands at 952 and 521 cm^{-1} to SiO_4 (Liu and Comodi, 1993; Khorari et al., 1994).

An interaction between the OH and F ions in the column was confirmed by clear OH stretching and vibrational bands in the IR spectrum. The OH bands shift from 3573 and 634 cm^{-1} in a pure hydroxylapatite to 3536 and 739 cm^{-1} in the Abruzzi apatite, which represents a typical O−H−F bond interaction in a binary OH-F apatite (Freund and Knobel, 1977).

As the structural carbonate v_3 bands near 1450 and 1420 cm^{-1} were hardly distinguishable, the carbonate was not regarded as important in the tetrahedral substitution.

Raman and RM spectroscopy

The Raman spectra of the investigated apatite samples contained bands resulting from each of the four phosphate internal vibrational modes and bands due to structural silicate and sulphate. The v_1 (PO_4) band at 962 cm^{-1} is extremely intense and represents the most noticeable feature of the Raman spectra. The v_2 (PO_4) mode was triply degenerate but in general only two bands at 427 and 445 cm^{-1} were resolved. Both the v_3 (PO_4) and v_4 (PO_4) modes degenerate in five bands. In the Durango fluorapatite the five components of the v_3 (PO_4) mode were clearly distinguished at 1080, 1060, 1052, 1041 and 1033 cm^{-1} (Liu et al., 1998), but in the Abruzzi samples the v_3 mode was represented by only two or three weak bands with a systematic weakening and broadening as the Si and S contents increase (see below). Generally, in the Abruzzi samples the v_4 (PO_4) mode occurred as three bands near 580, 590 and 606 cm^{-1}. As in the IR spectra, the bands due to the v_1 modes of SO_4 and SiO_4 were resolved clearly at 1007 and 865 cm^{-1}, respectively (Khorari et al., 1994). Moreover, we found a previously unreported band at 645 cm^{-1} in relatively highly S and Si substituted CG5, CG6,

CG1 samples (Fig. 2), the intensity of which was correlated with the content of S or Si. The same band at 641 cm^{-1} was found in the Raman spectrum of ellestadite. As bond order, which decreases in the series SO_4-PO_4-SiO_4, is responsible for the tetrahedral vibrational frequency variations: v_1 (SO_4), v_1 (PO_4) and v_1 (SiO_4) (Khorari *et al.*, 1994), it seemed reasonable to assign this band as a v_4 mode of sulphate. In the Raman spectrum of ellestadite, the following bands were resolved: four (SO_4) bands at 1004 (v_1), near 460 (v_2), near 1130 (v_3), and 620–640 (v_4) cm^{-1}; one (SiO_4) v_1 band at 853 cm^{-1}; and one (PO_4) v_1 band at 955 cm^{-1} (for band assignments see Arkhipenko and Moroz, 1997).

Discussion and concluding remarks

The chemical and spectral data indicate that the Abruzzi apatite is a hydroxyl–fluorapatite.

The most distinctive compositional feature of the Grotta del Cervo apatite is its unusually high S coupled with high Sr, *LREE* and Si. Since Na is negligible and varies independently of the *REE*, the coupled substitution of Na^+ and REE^{3+} for Ca^{2+}, such as occurs in the apatite from the Ilimaussaq alkaline intrusion (Ronsbo, 1989), may be regarded as unimportant from a crystal chemistry point of view. A positive correlation was found between the *LREE* plus S and Si content in the Abruzzi apatite (Fig. 3). If we define 100 (10−Ca)/Ca atoms per cell as the *Ca-site Substitution Index* (CSI), a clear direct relationship between CSI and the *Tetrahedral Substitution Index* (TSI = 100 (Si+S+C)/P atoms per cell, see Stoppa and Liu, 1995) can be observed (Fig. 4). However, sample CG5 falls outside the above pattern, implying that major substitution occurred in the tetrahedral site of this sample. The above compositional evidence indicates consistently that complex coupled substitutions occurred in both the tetrahedra and Ca polyhedra of the Abruzzi apatite, i.e. REE^{3+} + Si^{4+} = Ca^{2+} + P^{5+} and Si^{4+} + S^{6+} = 2 P^{5-} and Sr^{2-} = Ca^{2+}.

A comparison of the compositional and micro-Raman spectra from single crystals revealed the influences of substitution of Si and S for P on their vibrational behaviour. In their Raman study of synthetic solid-solution samples, Khorari *et al.* (1994) found that the relative intensity of SO_4 and SiO_4 v_1 bands (at 1007 and 865 cm^{-1} respectively) increased as Si and S substituted for P, whereas the five components of the v_3 PO_4 mode
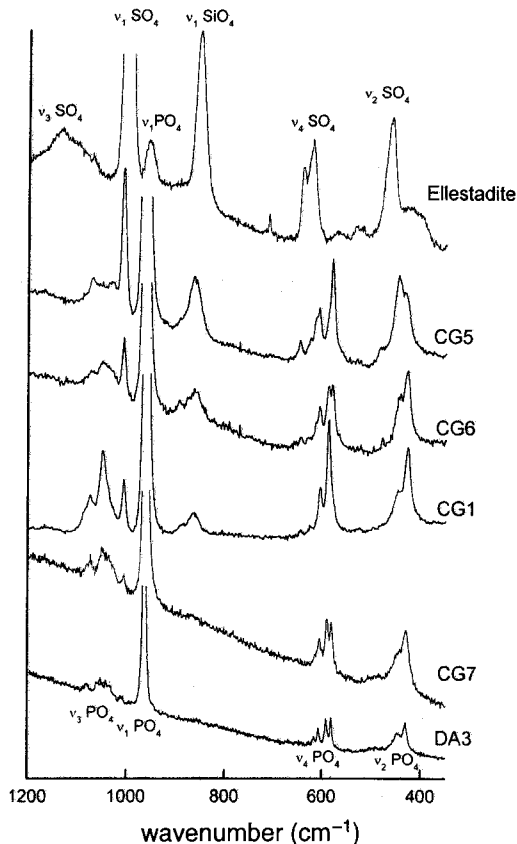

FIG. 2. Raman spectra of samples CG1, CG5, CG6 and CG7. Raman spectra of Durango apatite and ellestadite are also illustrated for comparison.

disappeared as a result of a progressive broadening and weakening. In the spectra of natural Si- and S-substituted apatite, we found the same relationship, i.e. as Si and S increase the bands of phosphate v_3 Raman mode (near 1020–1080 cm^{-1}) weaken and broaden from five well-distinguished bands in Durango fluorapatite, to three bands in CG7 and two bands in CG1. In the CG6 and CG5 samples with the highest Si and S contents (Table 1), the v_3 mode of phosphate showed only a hardly-distinguishable broad, weak hump, whereas the relative intensity of v_3 bands of SO_4 and SiO_4 increases (Fig. 2).

If we define integrated intensity ratios between the v_1 (SO_4) band and the v_1, v_2, v_3 and v_4 (PO_4) bands as $I_{(S/P1)}$, $I_{(S/P2)}$, $I_{(S/P3)}$ and $I_{(S/P4)}$, a clear positive correlation between these ratios and the
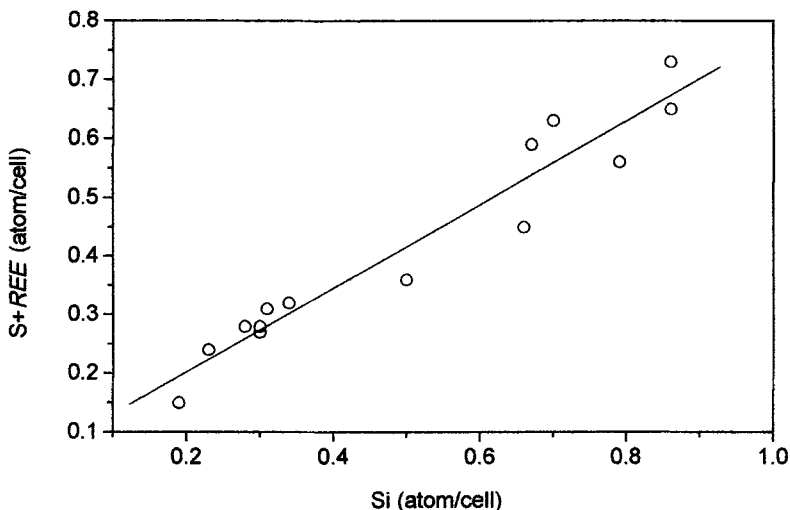
FIG. 3. Number of sum of *LREE* and S *vs* Si (atom/cell).

S/P atom/cell ratio can be observed (Fig. 5*a*). The same correlation occurs for bands of SiO_4 and PO_4 (Fig. 5*b*). With respect to other modes, a sharper increase occurs in the ratios $I_{(S/P3)}$, $I_{(Si/P3)}$ as S and Si increase. It seems that the stretching v_3 (PO_4) mode is more sensitive to the change of the polarization of cation-oxygen bonds in tetrahedra, resulting from Si and S substitutions for P.

Furthermore, we found a progressive broadening of the v_1 (PO_4) mode (at 962 cm^{-1}) and v_4 (PO_4) mode (with the strongest component at 590 cm^{-1}) with the substitution in tetrahedra. The widths at half-height of these bands are linearly correlated with Si+S atoms per cell (Fig. 6*a*). For the v_2 (PO_4) band the same relationship occurs, but with a more disperse band width. As for the v_3 (PO_4) band, a systematic weakening with the tetrahedral substitution inhibits a detailed discussion of its width.

As indicated by our structural refinements, tetrahedral substitution of Si and S for P not only changes the tetrahedral dimension but also increases the tetrahedral distortion. As Si and S substitute for P in the tetrahedra, the geometric distortion, in terms of quadratic elongation (QE) and tetrahedral angle variation (TVA), (Robinson *et al.*, 1971), increases (Liu and Comodi, 1993).

In a greatly distorted phosphate tetrahedron, the bond length and O—P—O bond angle vary greatly in different directions, resulting in a variation in P—O bond vibrational frequency. On the other

hand, as Si and/or S substitute for P, the vibrational interactions among these tetrahedral anions increase and result in a variation of their vibrational frequencies. Moreover, we found an increase of the width at half-height of the strongest v_1 (SO_4) band with S (Fig. 6*b*). It appears that the tetrahedral distortion and the vibrational interactions among the different tetrahedral anions may account for the systematic increase of the width of the (PO_4) and (SO_4) bands.

Multi—method analyses coupled with structural information allowed us to constrain elements which are sensitive to apatite-crystallizing melt,
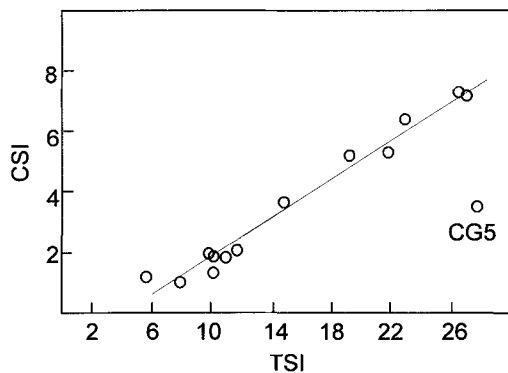

FIG. 4. Ca-site Substitution Index (CSI) *vs* Tetrahedral Substitution Index (TSI) in the Abruzzi apatite samples.
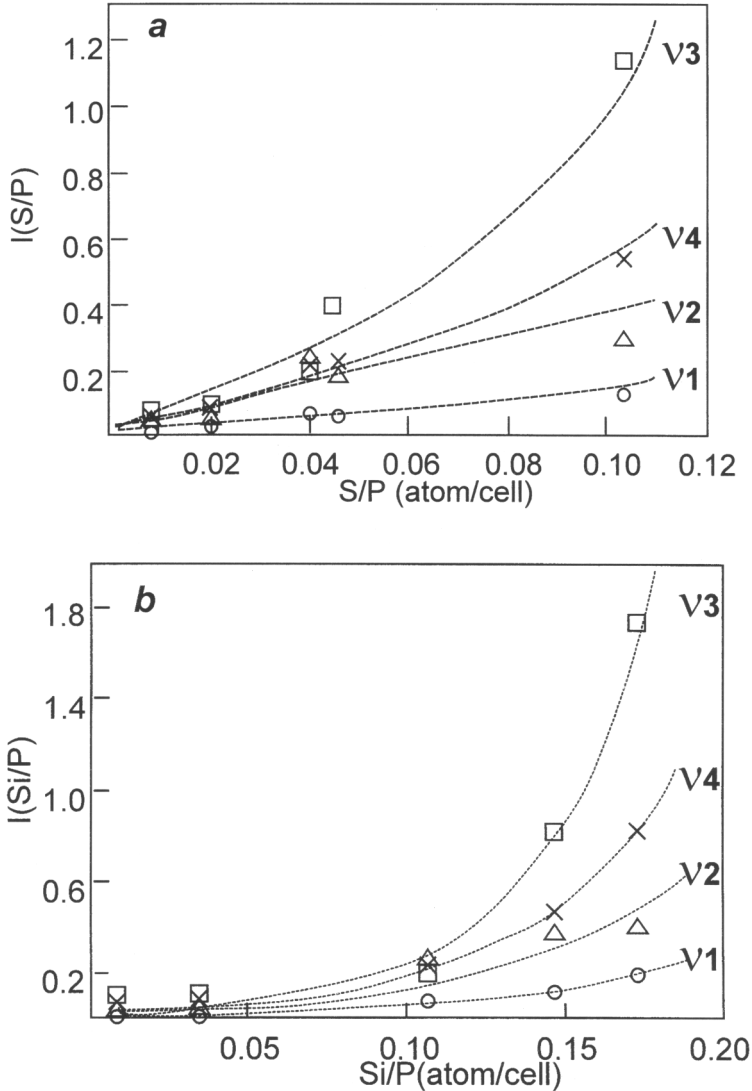
FIG. 5. (*a*) Intensity ratio of v_1 SO_4 and v_1, v_2, v_3, v_4 (PO_4) Raman bands (expressed as $I_{(S/P1)}$, $I_{(S/P2)}$, $I_{(S/P3)}$, $I_{(S/P4)}$, see text) *vs* S/P atom ratio in the cell. (*b*) Intensity ratio of $v_1(SiO_4)$ and v_1, v_2, v_3, v_4 (PO_4) Raman bands (expressed as $I_{(Si/P1)}$, $I_{(Si/P2)}$, $I_{(Si/P3)}$, $I_{(Si/P4)}$, see text) *vs*. Si/P atom ratio in the cell.

relative to elements which may be considered to enter the apatite structure as balancing factors in crystal chemical relationships. The observed substitution of *LREE* + Sr for Ca doesn't mirror SO_4 for PO_4. The SO_4 is constant in core and rim compositions but insensitive to dramatic increases of *LREE* + Sr toward the rim. A plot of the data on a P-Si-S triangle reveals that the Si/S ratio is

~1 in the core and >1 for the rim (Fig. 7). It indicates a major tetrahedral substitution of Si+S for 2P in the core, and a complex tetrahedral and Ca- polyhedral substitution of Si, S and *LREE* for 2P and Ca in the rim. Silicon is related to a *LREE* increase and enters the structure to balance the charge. As a consequence, only a high S content and a *LREE*+Sr increase are regarded as reflecting
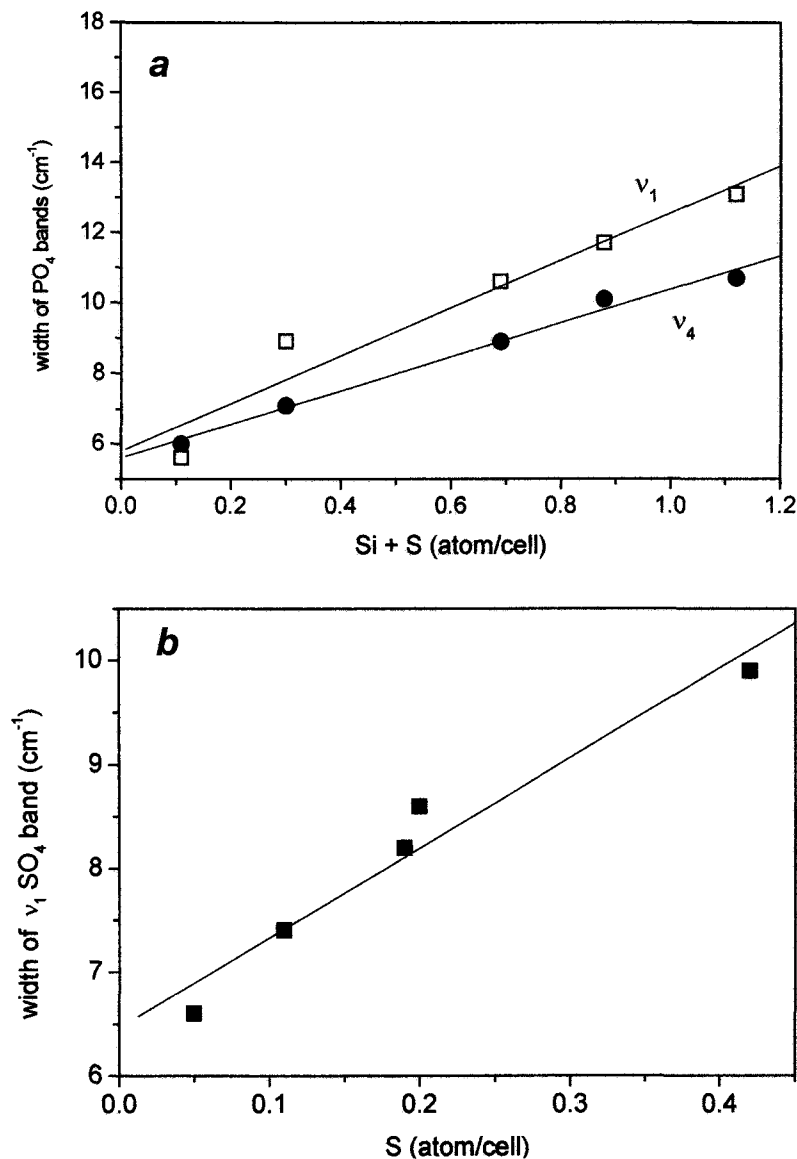
FIG. 6. (a) Width of v_1, v_4 (PO$_4$) Raman bands vs Si+S atom/cell. (b) Width of v_1(SO$_4$) Raman bands vs S atom/cell.

external causes such as melt evolution and crystallization conditions.

Acknowledgements

We would like to thank Professor P.F. Zanazzi for helpful suggestions during the preparation of the manuscript. We are also greatly indebted to Aldo Cundari for reviewing an early version of the manuscript. P. Sassi and G. Molin are kindly acknowledged for providing access to EMPA facilities at Padova University. Finally, we wish to express our warmest thanks to Terry Williams and John Spratt for their expert help during the probe work at the Natural History Museum, London. This work was supported by GNV
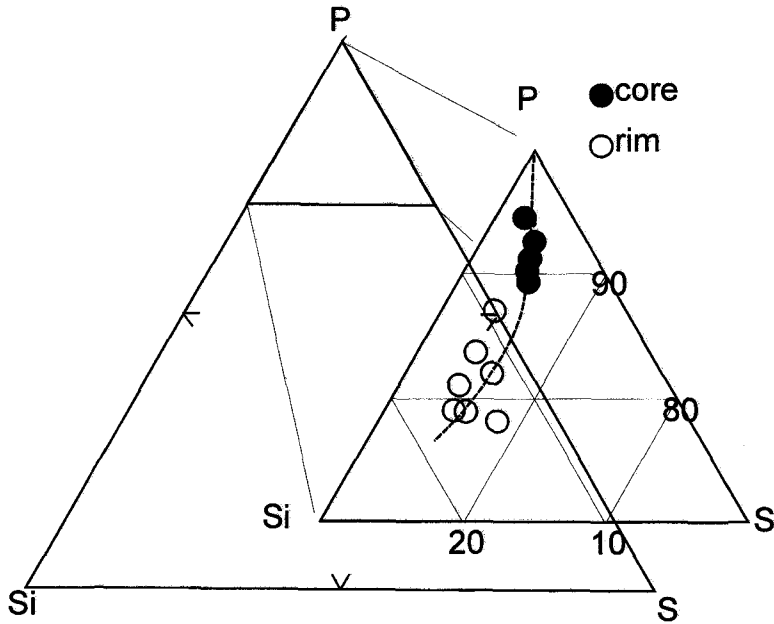
FIG. 7. P-Si-S component triangle of Grotta del Cervo apatite (normalized to P + Si + S = 6).

(96.00881.PF62) and MURST (project 'Relations between structure and properties in minerals: analysis and application').

References

Arkhipenko, D., and Moroz, T. (1997) Vibration spectrum of natural ellestadite. *Crystallogr. Rep.*, **42**, 651−6.

Deer, W.A., Howie, R.A., Zussman, J. and Chang, L.L.Y. (1996) *The Rock-forming Minerals*, 2nd edn, Geological Society, London, pp. 297−334.

Exley, R.A. and Smith, J.V. (1982) The role of apatite in mantle enrichment processes and in the petrogenesis of some alkaline basalt suites. *Geochim. Cosmochim. Acta*, **46**, 1375−84.

Farver, J.R. and Giletti, B.J. (1989) Oxygen and strontium diffusion kinetics in apatite and potential applications to thermal history determination. *Geochim. Cosmochim. Acta*, **53**, 1621−31.

Featherstone, J.D.B., Pearson, S. and LeGeros, R.Z. (1984) An infrared method for quantification of carbonate in carbonated apatites. *Caries Res.*, **18**, 63−6.

Fleet, M.E. and Pan Y. (1995) Site preference of rare earth elements in fluoroapatites. *Amer. Mineral.*, **80**, 329−35.

Fleet, M.E. and Pan Y. (1997) Site preference of rare earth elements in fluoroapatite: Binary (LREE+HREE)-substituted crystals. *Amer. Mineral.*, **82**, 870−7.

Freund, F. and Knobel, R.M. (1977) Distribution of fluorine in hydroxy-apatite studied by infrared spectroscopy. *J. Chem. Soc., Dalton Trans.*, **12**,1136−8.

Hughes, J.M. and Drexler, J.W. (1991) Cation substitution in the apatite tetrahedral site: crystal structures of type hydroxylellestadite and type fermorite. *Neues. Jahrb. Mineral. Mh.*, H7, 327−36.

Hughes, J.M., Cameron, M. and Crowley, K.D. (1989) Structural variations in natural F,OH, and Cl apatites. *Amer. Mineral.*, **74**, 870−6.

Hughes, J.M., Cameron, M. and Crowley, K.D. (1991) Ordering of divalent cations in the apatite structure: crystal structure refinements of natural Mn- and Sr-bearing apatite. *Amer. Mineral*, **76**, 1857−62.

International Tables for X-ray Crystallography (1974) Vol. 4, Kynoch Press, Birminghan, England.

Khorari, S., Cahay, R., Rulmont, A. and Tarte, P. (1994) The coupled isomorphic substitution $2(PO_4)^{3-} =$ $(SO_4)^{2-} + (SiO_4)^{4-}$ in synthetic apatite $Ca_{10}(PO_4)_6F_2$: a study by X-ray diffraction and vibrational spectroscopy. *Eur. J. Sol. St. Inorg. Chem.*, **31**, 921−34.

Klee, W.E. (1970) The vibrational spectra of the

phosphate ions in fluorapatite. *Zeits. Kristallogr.*, **131**, 95−102.

Kravitz, L.C., Kingsley, J.D. and Elkin, E.L. (1968) Raman and Infrared studies of coupled PO_4^{3-} vibrations. *J Chem. Phys.,* **49**, 4600−10.

Lavecchia, G., Stoppa, F. (1996) The tectonic significance of Italian magmatism: an alternative view to the popular interpretation. *Terra Nova*, **8**, 435−46.

Liu, Y. and Comodi, P. (1993) Some aspects of the crystal-chemistry of apatites. *Mineral. Mag.*, **57**, 709−19.

Liu, Y., Comodi, P. and Sassi, P. (1998) Vibrational spectroscopic investigation of phosphate tetrahedron in fluor-, hydroxy-, and chlorapatites. *Neues. Jahrb. Miner. Abh.*, **174/2**, 211−22.

Nash, W.P. (1983) Phosphate minerals in terrestrial igneous and metamorphic rocks. In *Phosphate Minerals* (J.O. Nriagu and P.B. Moore, eds) Springer-Verlag, Berlin and New York, pp. 215−41.

North, A.C.T., Phillips, D.C. and Mathews, F.S. (1968) A semi-empirical method of absorption correction. *Acta Crystallogr.*, **A24**, 351−9.

Regnier, P., Lasaga, A.C., Berner, R.A., Han, O.H. and Zilm, K.W. (1994) Mechanism of CO_3^{2-} substitution in carbonate-fluorapatite: evidence from FTIR spectroscopy, ^{13}C NMR, and quantum mechanical calculations. *Amer. Mineral.*, **79**, 809−18.

Roeder, P.L., MacArthur, D., Ma, X.P. and Palmer, G.R. (1987) Cathodoluminescence and microprobe study of rare-earth elements in apatite. *Amer. Mineral.*, **72**, 801−11.

Robinson K., Gibbs G.V. and Ribbe P. H. (1971) Quadratic elongation: a quantitative measure of distortion in coordination polyhedra. *Science*, **172**, 567−70.

Ronsbo, J.G. (1989) Coupled substitutions involving REEs and Na and Si in apatites in alkaline rocks from the Ilìmaussaq intrusion, South Greenland, and the petrological implications. *Amer. Mineral.*, **74**, 896−901.

Rouse, R.C. and Dunn, P.J. (1982) A contribution to the crystal chemistry of ellestadite and the silicate sulphur apatites. *Amer. Mineral.*, **67**, 90−6.

Santos, R.V. and Clayton, R.N. (1995) The carbonate content in high-temperature apatite: an analytical method applied to apatite from the Jacupiranga alkaline complex. *Amer. Mineral.*, **80**, 336−44.

Sheldrick, G.M. (1993) *SHELXL93, program for the refinement of crystal structure.* University of Gottingen, Germany.

Stoppa, F. and Liu, Y. (1995) Chemical composition and petrogenetic implications of apatites from some ultra-alkaline Italian rocks. *Eur. J. Mineral.*, **7**, 391−402.

Watson, E.B. and Green, T.H. (1981) Apatite/liquid partition coefficients for the rare earth elements and strontium. *Earth Planet. Sci. Lett.*, **56**, 405−21.

Young, E.J., Myers, A.T., Munson, E.L. and Conklin, N.M. (1969) Mineralogy and geochemistry of fluorapatite from Cerro de Mercado, Durango, Mexico. *U.S. Geol. Surv. Res.,* **650**−**D**, D84−D83.